Giga-LES of Hector the Convector and Its Two Tallest Updrafts up to the Stratosphere

Thibaut Dauhut, Jean-Pierre Chaboureau, Juan Escobar, Patrick Mascart

Giga-LES of Hector the Convector and Its Two Tallest Updrafts up to the Stratosphere

THIBAUT DAUHUT, JEAN-PIERRE CHABOUREAU, JUAN ESCOBAR, AND PATRICK MASCART

Laboratoire d'Aérologie, Université de Toulouse, CNRS, UPS, Toulouse, France

(Manuscript received 11 March 2016, in final form 8 September 2016)

ABSTRACT

The dynamics of Hector the Convector, which overshot into the stratosphere on 30 November 2005 over the Tiwi Islands, Australia, is investigated using a giga-large-eddy simulation with a 100-m cubic mesh. Individual updrafts, defined as 3D objects with vertical velocity above 10 m s^{-1} are identified. Among the 20 000 updrafts formed during the most intense phase, only a dozen were more than 4 km tall. The two tallest updrafts accounted for more than 90% of the total vertical mass flux through the tropical tropopause layer. Their locations were determined by low-level convergence lines first created by the sea breeze in the morning, then enhanced by cold pools due to cumulus congestus. They finally reinforced each other as they moved inland and intersected. The two tallest updrafts that overshot the tropopause were contrasted with those occurring 1 h earlier and later. They presented larger widths (up to 8 km), greater buoyancy (up to 0.1 m s^{-2}), stronger vertical velocities (up to 50 m s^{-1}), and larger hydrometeor contents (more than 10 g kg^{-1}). They kept their core weakly diluted on their way to the stratosphere with an entrainment rate as low as 0.08 km^{-1}. Both the low-level convergence lines intensified by cold pools and the reduced mixing in the troposphere were found to be the determinant for the transition from deep to very deep convection.

1. Introduction

In the tropics, the very deep convective systems are so deep that they cross the tropical tropopause layer (TTL) and reach the stratospheric overworld (Holton et al. 1995). Because of their supposed scarcity, the capacity of very deep convective events to redistribute low-troposphere species into the stratosphere has long been considered negligible. Recent observations have attracted renewed attention to the role of very deep convection on the stratosphere composition. Ice particles were found in the lower stratosphere above continental Brazilian thunderstorms (Chaboureau et al. 2007; Nielsen et al. 2007) and over the famous thunderstorm Hector the Convector in Australia (Corti et al. 2008; de Reus et al. 2009). Associated cloud-resolving model (CRM) simulations were successful in simulating very deep convection (e.g., Chaboureau et al. 2007; Chemel et al. 2009; Liu et al. 2010). Dauhut et al. (2015) performed a series of large-eddy simulations (LESs) and CRM simulations of Hector. They found a stratosphere hydration of 3000 tons (1 ton ≈ 1000 kg) over the storm episode, almost converging at 100- and 200-m horizontal grid spacings. Upscaling this hydration, they estimated the contribution of very deep convection to the troposphere-to-stratosphere water mass flux at 18%. This result suggests that the very deep convection can have a large impact on the composition of the stratosphere.

An aspect of Hector not investigated so far is its internal organization that leads to the stratosphere hydration. Hector the Convector is a multicellular thunderstorm that develops on an almost daily basis during the premonsoon period (November and December) above the Tiwi Islands, 100 km north of Darwin, Northern Australia (Keenan et al. 1989). Its regularity makes it a natural laboratory and the subject of many studies investigating the triggering of the most intense convection (Crook 2001; Saito et al. 2001; Ferretti and Gentile 2009), the microphysical properties of overshooting convection (Frey et al. 2014), and the sensitivity of its representation to models (Chemel et al. 2009) and to their resolution (Dauhut et al. 2015). The last four studies focused on the event of 30 November 2005, documented during the

Corresponding author address: Thibaut Dauhut, Laboratoire d'Aérologie, Observatoire Midi-Pyrénées, 14 Ave. Edouard Belin, 31400 Toulouse, France.
E-mail: thibaut.dauhut@aero.obs-mip.fr

DOI: 10.1175/JAS-D-16-0083.1

Stratospheric-Climate Links with Emphasis on the Upper Troposphere and Lower Stratosphere (SCOUT-O3) campaign (Brunner et al. 2009). On that day, Hector comprised two main cells: the first was apparently triggered by the intersection of two sea-breeze fronts in the east of the islands and the second by the encounter of the gusts produced below the first cell with another sea-breeze front (Ferretti and Gentile 2009). Some pockets of ice crystals were observed to be injected into the stratosphere by Hector (Corti et al. 2008; de Reus et al. 2009).

The goal of this article is to investigate the key processes that led the thunderstorm to overshoot into the stratosphere. The internal structure of Hector is investigated in terms of individual updrafts. The updrafts are the elementary structures of the active parts of the system, where air masses ascend faster than anywhere else. Previous studies have considered the updrafts all together and computed their statistical properties inside the whole volume of the updrafts (e.g., Khairoutdinov et al. 2009; Romps and Kuang 2010; Dauhut et al. 2015). Here, each individual updraft is identified through the application of a clustering algorithm. It is then possible to compute statistics on the population of updrafts, to detect any outstanding structures that enable Hector to reach the stratosphere, and to characterize them. In the following, it will be shown that the two tallest updrafts are those that matter for the hydration of the stratosphere.

The first question concerns the formation and the properties of the tallest updrafts that reach the tropopause. The mechanisms leading to the triggering and development of Hector will be investigated in detail. The second question addresses the efficiency of the transport toward the stratosphere. In particular, two characteristics determine how efficient the transport is: the vertical mass flux of the updrafts and the entrainment of environmental air. The latter measures how much the updrafts are diluted by the environment during their ascent in the atmosphere.

How this dilution affects the planetary boundary layer (PBL) air rising to the stratosphere is a long-debated question. The existence of very tall updrafts with almost no dilution by environmental air was first postulated by Riehl and Malkus (1958). However, since this pioneering work, many CRM studies have shown the existence of dilution for updrafts. Typical midtroposphere values of entrainment around $0.2\,\mathrm{km}^{-1}$ have been found for different deep convective cases (e.g., Khairoutdinov and Randall 2006; Del Genio and Wu 2010; de Rooy et al. 2013). In general, the entrainment rate is reduced with increasing convection depth (Del Genio and Wu 2010). The intensity of the entrainment is also lower in the middle of the updraft vertical extension, while larger values are found at the base (Del Genio and Wu 2010; de Rooy et al. 2013). A numerical study in radiative–convective equilibrium attested to the virtual absence of undiluted PBL air at the tropopause and even at the freezing level (Romps and Kuang 2010). Instead, the capacity of the updrafts to overshoot the tropopause was attributed to the boost given by the release of latent heat due to the freezing of hydrometeors. For this Hector case of very deep convection, we will show the existence of two tall updrafts that experienced the least dilution ever evidenced and accounted for most of the vertical mass flux into the stratosphere.

The use of a giga-LES in this study is worth emphasizing. A few LESs of deep convection have been run so far: a shallow-to-deep transition over land (Khairoutdinov and Randall 2006), a maritime deep convection in near equilibrium (Khairoutdinov et al. 2009), and Hector the Convector (Dauhut et al. 2015). These studies show that the cumuli are quickly diluted by the mixing with the environment during the shallow convection phase. This quick dilution, a scale-aware process, affects the time needed by the convection to deepen. As a result, the updraft core velocities and total water content are larger at finer resolutions. This points out the need for a minimum of 100- or 200-m grid spacing to resolve the convective flow properly in a deep convective system.

This article is organized as follows. The simulation setup and the clustering method are described in section 2. The time evolution of the thunderstorm and its updrafts is characterized in section 3, where the importance of the tallest updrafts is shown. The formation, the properties, and the mass transport of these tallest updrafts are investigated in section 4. The key processes leading to very deep convection are summed up in section 5, where perspectives for future work are also suggested.

2. Model design and clustering approach

a. *Meso-NH large-eddy simulation*

The simulation (Dauhut et al. 2015) was performed with the anelastic nonhydrostatic mesoscale model Meso-NH (Lafore et al. 1998). The domain of simulation extended over a surface of $256 \times 204.8\,\mathrm{km}^2$ centered over the Tiwi Islands (Fig. 1). Such a wide domain was chosen to avoid deep convection being affected by open conditions imposed at lateral boundaries. In the vertical, the model had 256 levels up to 25-km altitude to include the whole TTL and the lower stratosphere, with a damping layer in the uppermost 3 km. In the horizontal, the grid spacing was set at 100 m to resolve the most energetic eddies explicitly. With a computational domain of 1.34 billion grid points ($2560 \times 2048 \times 256$), this so-called giga-LES was made possible thanks to the adaptation of

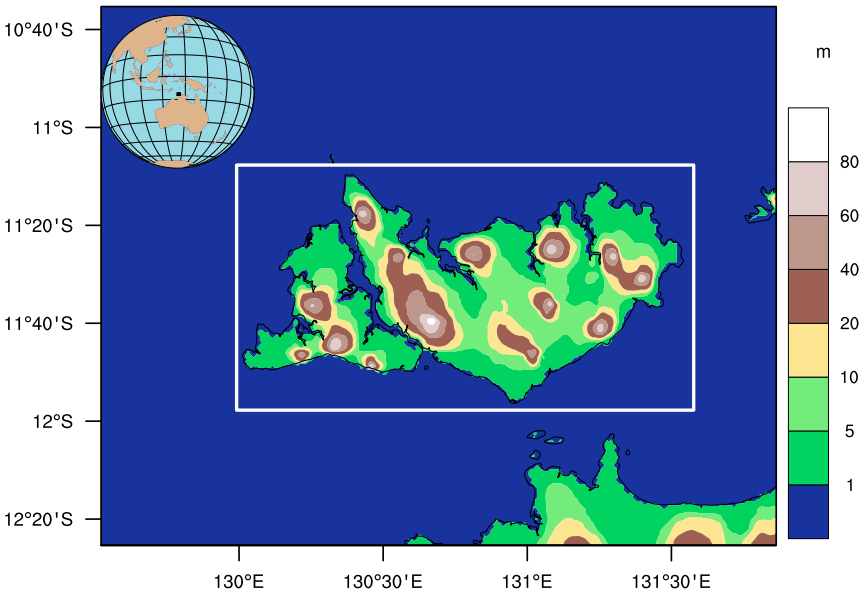

FIG. 1. Domain of simulation. The white rectangle is the domain of analysis, centered above the Tiwi Islands (Bathurst and Melville Islands to the west and east, respectively). The black lines are the coastlines. The color shades indicate the altitude above sea level.

Meso-NH for massively parallel computing (Pantillon et al. 2011). It was run for 10 h using 16 384 cores on an IBM Blue Gene/Q. The prognostic model variables were saved every 15 min, generating 20 Tb of data. Physical parameterizations included a 3D turbulence scheme based on 1.5-order closure (Cuxart et al. 2000), a mixed-phase microphysical scheme (Pinty and Jabouille 1998), the radiative scheme used at the European Centre for Medium-Range Weather Forecasts (ECMWF; Gregory et al. 2000), and the Interactions between Soil, Biosphere and Atmosphere (ISBA) scheme (Noilhan and Planton 1989).

The sounding (Fig. 2) launched from Darwin at 0930 LST (0000 UTC) 30 November 2005 was used for the initial conditions. The convective available potential energy was 2074 J kg^{-1}. We extended the water vapor profile between 13 and 17 km with the water vapor content from the ECMWF analysis. Above 17 km, based on observations by Corti et al. (2008), the water vapor content increased from 2 ppmv at 380 K (17 km) to 4 ppmv at 410 K (18 km) and took a uniform 4-ppmv value aloft. No large-scale forcing was applied. The description of orography and land cover was obtained from 1-km-resolution databases in order to remain the same when applied to coarser-resolution simulations (Dauhut et al. 2015). A sea surface temperature of 29°C, a surface soil temperature of 30°C, and a moisture content of 0.16 m^3 m^{-3} taken from the ECMWF analysis were used for surface initial conditions. Over the ocean, the sea surface temperature was kept constant with time. As a consequence, the change in air–surface fluxes was due to the variation in atmospheric temperature and wind only. Over land, the surface fluxes were computed by the ISBA scheme. This allows the land surface fluxes to evolve in time with the change of both soil and atmospheric variables.

To explore the sensitivity of Hector's properties to the horizontal resolution, we performed additional simulations

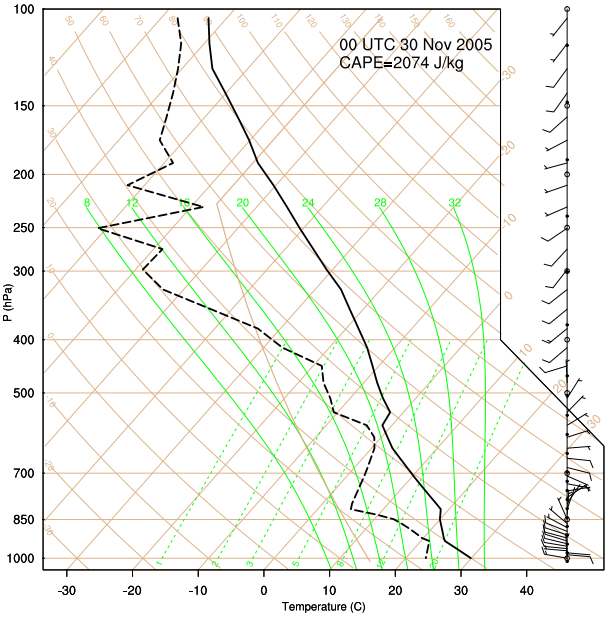

FIG. 2. Atmospheric profiles of temperature (solid line) and dewpoint temperature (dashed line) from the sounding taken in Darwin at 0930 LST 30 Nov 2005.

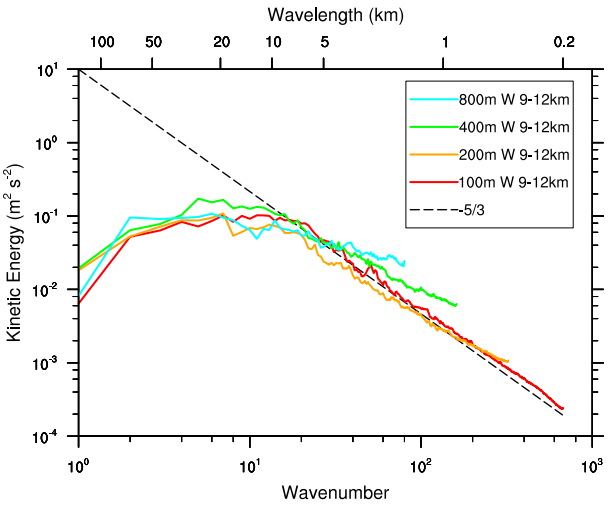

FIG. 3. Spectra of vertical motions at 1400 LST at 9–12-km altitudes in the LES (100-m grid spacing), the 200-, 400-, and 800-m simulations. The theoretical power law at −5/3 is shown with the black dashed line.

with grid spacings of 200, 400, and 800 m using the same parameterizations, domain, and integration time. These simulations at coarser resolutions also reproduced Hector's overshoots and its water transport into the lower stratosphere (Dauhut et al. 2015). The vertical velocity distributions were relatively robust with the resolution for the grid spacings between 100 and 800 m. They all showed 90th-percentile profiles of the upward wind velocity departing one from the other of less than 2 m s^{-1}. At 1300 LST, the spectra of the vertical motions between 9 and 12 km of altitude were compared to the theoretical spectrum (Fig. 3). For all resolutions, the kinetic energy contained in the vertical motions ranging from 7.5- to 75-km horizontal scale was almost constant, on the order of 10^{-1} m^2 s^{-2}. At smaller horizontal scales, the kinetic energy decreased following the theoretical power law of −5/3. For the 400- and the 800-m grid spacings, the smallest scales contained too much kinetic energy compared to the theoretical spectrum. This suggests a lack of energy dissipation by the turbulence scheme for these grid spacings. In contrast, the spectra of vertical motions for the simulations with 100- and 200-m grid spacings fit the theoretical spectra very well for wavelengths shorter than 5 km. This shows that the vertical motions were well resolved down to a wavelength of 200 m for the LES. In the rest of the study, only the LES output (100-m grid spacing) will be considered.

b. *Updraft cluster identification*

We define updrafts as three-dimensional objects made of connected grid points for which the vertical velocity exceeds an arbitrary threshold. Once detected and identified, these objects can be described individually by computing geometrical, thermodynamical, and dynamical properties. Updraft cluster identification consists in distinguishing the different updrafts and in giving a different identity number to each. In practice, two grid points of the atmosphere have the same updraft identity number if and only if they belong to the same updraft: that is, there is a path connecting them where the vertical velocity is over the threshold. Two criteria define our cluster identification: the vertical velocity threshold and the rules of connectivity.

The vertical velocity threshold is assumed to be large enough so that local fluctuations of the vertical velocity will not be considered as updrafts and that the updrafts are properly separated from one another. A threshold of 1 m s^{-1} is commonly used (e.g., Khairoutdinov et al. 2009; Romps and Kuang 2010; Glenn and Krueger 2014) but accompanied by a threshold on condensed water content. In cases of very deep convection like Hector the Convector, strong gravity waves are excited (Lane et al. 2001), producing fluctuations of vertical wind in the upper troposphere and in the stratosphere, which must not be mistaken for updrafts. They reach a maximum amplitude of 4 m s^{-1}, which is much less than the strongest updrafts. Since the LES presents very large values of vertical velocity, up to 8 m s^{-1} for the 90th percentile and 22 m s^{-1} for the 99th percentile of the vertical velocities over 1 m s^{-1} (Dauhut et al. 2015), we selected a threshold of 10 m s^{-1}. Visual inspection supported this choice for the detection of updrafts.

The rules of connectivity determine the shape of the updrafts. Two contiguous grid points (i.e., sharing a common face either in the horizontal or the vertical direction) are considered as connected. Diagonal connections are considered only in the vertical direction in order to take slantwise convection into account.

As the LES has more than 1 billion grid points, the updraft cluster identification had to be run on parallel computers for practical efficiency. The MPI library was used for communication between processors. We applied the updraft cluster identification algorithm to the snapshots of the whole 3D simulated volume (available every 15 min) every time deep convection occurred. An example is given at 8-km altitude, at 1315 LST (Fig. 4a). The updrafts occupy only a small part of the cloud section. The 10 largest updrafts can be identified, the smaller ones being too small to be noticed at the scale of the islands. The whole population at this time, more than 16 000 updrafts distributed between around 1- and 18-km altitudes, was represented in terms of vertical extent versus base altitude, volume, maximal effective width, and base effective width (Figs. 4b–e). The effective width is the diameter of a circle having the same

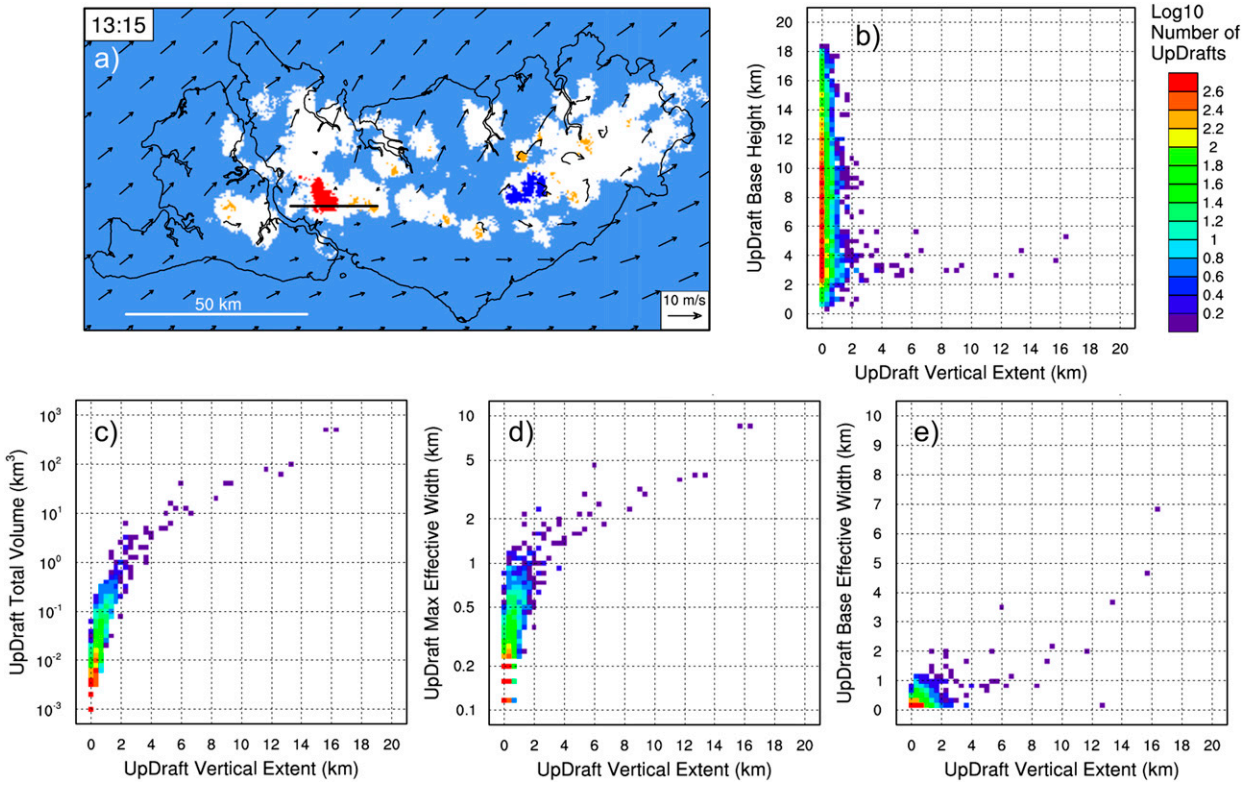

FIG. 4. LES outputs at 1315 LST. (a) Horizontal cross section of cluster identity numbers at 8-km altitude over the analysis domain. The two tallest updrafts are in blue and red, and the others are in orange. The clear sky is in light blue, and the cloud section is in white (cloud content above 10 mg kg^{-1}). The arrows represent the horizontal wind at 8-km altitude. The straight black line corresponds to the position of the vertical cross section shown in Fig. 9b. Histograms of updraft population in terms of vertical extent (x axis) (1/3-km bin intervals) vs (b) altitude of their base (1/3-km bin intervals), (c) their total volume (1/10 logarithmic bin intervals), (d) their maximal effective width (1/30 logarithmic bin intervals), and (e) effective width of their base (1/6-km bin intervals). The color shading gives the logarithmic number of updrafts in each bin.

area as the cross section of the updraft. Two main subpopulations were distinguished: short updrafts with a vertical extent of less than 4 km (the vast majority) and tall updrafts with a larger vertical extent (the remaining updrafts, between 10 and 20). The presence of the two different subpopulations was robust whatever the threshold on the vertical velocity. The short updrafts were characterized by a volume lower than 10 km^3, a maximal effective width lower than 3 km, and a base effective width lower than 2 km. The tall updrafts had a base below 6-km altitude, most of them even below 4-km altitude. The tall updrafts were contrasted from the short updrafts with a larger volume, most of them with a larger maximal effective width (up to more than 8 km), and a quarter of them with a significantly larger base effective width (up to 7 km). The two tallest updrafts, around 16 km tall, had the largest values of volume (both around 500 km^3), maximal effective width (both 8.7 km), and base effective width (6.9 and 4.7 km for the tallest and the second tallest updrafts, respectively). These very large horizontal extents, even at the base, found for the tallest updrafts, suggest that a large effective width is a property that characterizes them. Indeed, the effective widths at the base of the tallest updrafts were found limited up to 4 km for the rest of the time. The relation between the large horizontal extent and the dilution of the tallest updrafts needs to be investigated. The current study addresses this question by computing the effective entrainment rate of the tallest updrafts and by quantifying the transport of conserved variables inside the tallest updrafts. First, the importance of the two tallest updrafts during the whole time deep convection occurred is highlighted in section 3b. Their characteristics are then investigated in section 4.

3. Overview

a. *Main features*

The life cycle of Hector reproduced by the LES, and in particular its gradual growth toward the stratosphere,

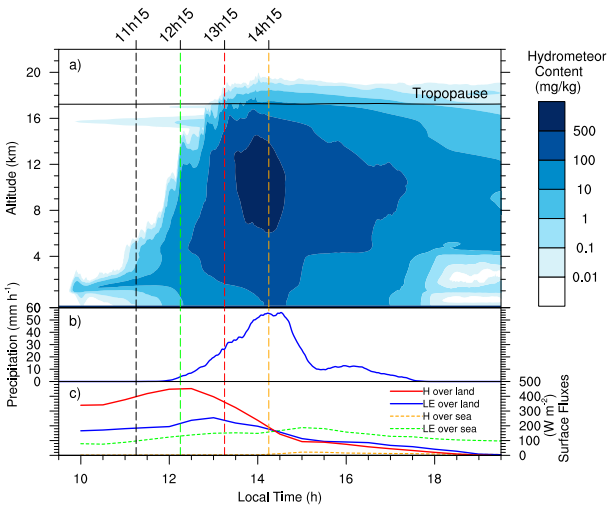

FIG. 5. Temporal evolution of (a) hydrometeor content, (b) precipitation rate at the surface, and (c) surface fluxes. In (c), sensible and latent heat fluxes are in red and blue solid lines over the islands and in orange and green dashed lines over the ocean, respectively. The key moments representative of the congestus, deep, very deep, and mature convection phases are highlighted with the black, green, red, and orange vertical dashed lines, respectively.

are shown in Fig. 5. The vertical profile of the hydrometeor content, the precipitation, and the surface fluxes, all averaged over the analysis domain shown in Fig. 1, allow the time evolution of Hector to be characterized with different phases, most during one hour.

The preconditional phase spanned from the beginning of the simulation to 1115 LST. The increase of surface fluxes over land first yielded dry convection over the Tiwi Islands. Cumulus humilis then appeared at the top of the PBL from 1000 LST. In agreement with the study by Saito et al. (2001), visual inspection of horizontal sections of the wind components (not shown) revealed that convective rolls formed on the windward (west) side of the islands from 1030 LST and that the sea breeze, as a result of the contrast in surface heat fluxes over land and sea, deflected the westerlies toward the Tiwi Islands (the wind slightly rotated toward the islands along the northern and the southwestern coasts, and its amplitude dramatically decreased along the southeastern coast: i.e., the lee shore). At 1115 LST, the congestus phase began with the first cumulus congestus reaching the freezing level, around 5-km altitude. The precipitation became significant, on the order of 2 mm h^{-1}, from 1200 LST as some cumulus congestus passed the freezing level and reached an altitude of 10 km.

The deep convection phase appeared at 1215 LST, with cumulonimbus tops around 14-km altitude, the lower bound of the TTL. The sensible heat flux over the islands was then maximum. During the following hour, the precipitation increased steadily, reaching 25 mm h^{-1}. At the surface of the islands, the sensible heat flux decreased back to its morning value, whereas the latent heat flux increased up to a maximum of 250 W m^{-2}. Meanwhile, the growth of deep convection showed two gradual stages. First, the cumulonimbus tops stayed at around 14 km for half an hour and then reached 16 km for another half hour. At 1315 LST, the very deep convection phase started as cumulonimbus overshot the tropopause (defined here by the 380-K potential temperature, which corresponds to the climatological cold-point tropopause situated around 17 km). During the following hour, the hydrometeor content steadily increased both in the stratosphere and in the troposphere, while the precipitation increased drastically up to 56 mm h^{-1}, and the sensible and latent heat fluxes decreased to 180 W m^{-2} over the islands.

From 1415 LST onward, Hector lost its vigor. The hydrometeor content in the troposphere decreased. The precipitation remained at its highest value for half an hour and then decreased sharply to 10 mm h^{-1}. At the surface, the heat fluxes continued to decrease over the islands, whereas they increased over the ocean because of the cold pools. In the stratosphere, the hydrometeor content decreased slowly as a result of sedimentation of ice particles. From 1515 LST onward, Hector was a more-stratiform-than-convective cloud system as the vertical velocity was strongly reduced (not shown). The precipitation rate remained almost steady (around 14 mm h^{-1}) for 1 h and then slowly decreased to zero at 1730 LST. Below the freezing level, the hydrometeor content decreased significantly between 1700 and 1800 LST, to almost zero thereafter. Aloft, the stratiform cloud in the troposphere and the hydrometeor content in the stratosphere decreased slowly, as a result of evaporation and advection out of the analysis domain.

We selected 1115, 1215, 1315, and 1415 LST as key moments, representative of the congestus, deep, very deep, and mature convection phases, respectively. The evolution of the updraft population during the deep, very deep, and mature convection phases is described in section 3b. The shape and properties of the tallest updrafts are studied in section 4.

b. *Updraft population*

The identification of the updrafts over the whole domain resulted in large populations of three-dimensional objects with very diverse sizes and properties. The evolution of their number, their geometry, and their mass flux through the freezing level and the base of the TTL is shown in Fig. 6. All characteristics show a similar

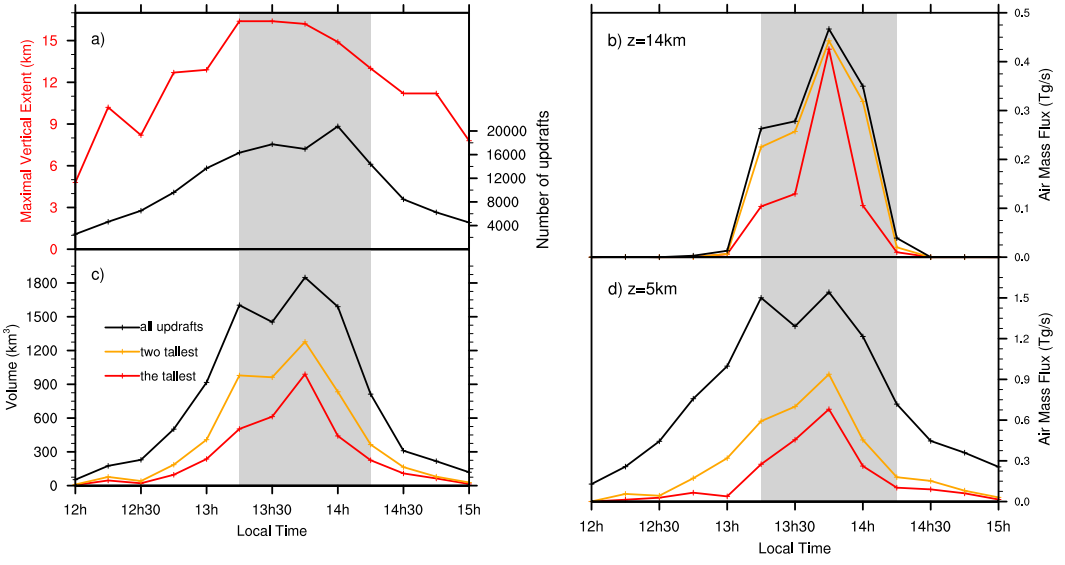

FIG. 6. Evolution of updraft characteristics: (a) maximal vertical extent in red and number of updrafts in black, (c) volume of the updrafts, and vertical air mass flux at (d) 5- and (b) 14-km altitude. The very deep convection phase is shaded in gray. In (b)–(d), the values for all the updrafts, the two tallest updrafts, and the tallest updraft are in black, orange and red, respectively.

evolution in the early afternoon, with an increase during the deep convection phase, a peak during the very deep convection phase, and a decrease during the mature convection phase. There were around 10 000 updrafts during the three phases, but most of them were extremely short (less than 333 m tall, for instance, at 1315 LST in Fig. 4b). Among the few tall updrafts, the two tallest ones had similar vertical extents and, most of the time, they were at least 2 km taller than the others. We now focus on their contribution to the volume and to the air mass flux in order to determine whether they were the most important coherent structures in the vertical transport.

After an intermittent increase during the deep convection phase, the maximal vertical extent reached its largest value of around 16 km and then remained constant for half an hour (Fig. 6a). The number of updrafts increased steadily until the end of the very deep convection phase, when it peaked around 20 000. During the mature convection phase, Hector experienced a decrease of the maximal extent of its updrafts, back to deep convection values (around 11 km), and a dramatic decrease in their number, which divided by 5 in 1 h, because of the decreasing convective activity (Fig. 5a).

The total volume of the updrafts (Fig. 6c) increased sharply during the deep convection phase (multiplied by 8 in 1 h), peaked at 1800 km^3 during the very deep convection phase, and decreased sharply during the mature phase (divided by 10 in 1 h). The increase in volume is representative of the growth of Hector in the vertical direction, whereas the decrease shows its weakening without any change in its vertical extent (see the hydrometeor content in Fig. 5a). Interestingly, the two tallest updrafts accounted for more than 60% of the total volume during the very deep convection phase and around 40% the rest of the time.

The air mass flux due to all the updrafts just above the freezing level (at 5-km altitude; Fig. 6d) was around 1.4 $Tg\,s^{-1}$ during the very deep convection phase. The contribution of the two tallest updrafts then accounted for 40%–60%. At 14-km altitude (corresponding to the base of the TTL), the air mass flux was truly significant during the very deep convection phase only, 0.34 $Tg\,s^{-1}$ on average. It is noteworthy that the contribution of the two tallest updrafts accounted for 91% on average. At 1315 and 1400 LST, the second tallest updraft contributed even more than the tallest.

The very deep convection phase exhibited a maximum in the number of updrafts, their vertical extent, their volume, and their air mass flux at different levels. The values during the deep and mature convection phases were lower but still significant for all properties, except for the flux through the base of the TTL. This flux characterized the ability of Hector the Convector to affect the composition of the TTL and the stratosphere. The two tallest updrafts contributed 91% of this flux, demonstrating that they were far more important than the other updrafts. It is of key importance to understand why and how such updrafts form and what gives them the ability to transport low-tropospheric air into the

TTL and the stratosphere. The following section tackles these questions.

4. Characteristics of the tallest updrafts

a. Development

As shown in the following, the tallest updrafts appear above areas of large moisture flux horizontal convergence. The latter are organized into lines of large positive values in the PBL, called convergence lines here. Maps of the moisture flux horizontal convergence at 210 m above the surface (where they are best defined), together with maps of the potential temperature at the first model level (20 m above the surface), are shown for the congestus, deep, very deep, and mature convection phases (Fig. 7). For the congestus phase, the formation of convergence lines is demonstrated using vertical sections of the tallest updraft across a line perpendicular to the coast (Fig. 8). For the deep, very deep, and mature convection phases, vertical cross sections of the tallest updrafts are represented (Fig. 9). Vertical profiles of the atmosphere 15 min before the development of these updrafts are examined in Fig. 10.

At 1115 LST, the congestus phase started. The near-surface potential temperature (Fig. 7a) was 2 K higher over the islands than over the ocean because of the contrast in sensible heat flux that exceeded 300 $W m^{-2}$. The sea breeze developed for about 45 min and led to the convergence of the horizontal wind at the scale of the islands. Local values of moisture flux horizontal convergence over 3 $g m^{-3} min^{-1}$ were reached along the coasts, forming early convergence lines (Fig. 7b). Vertical sections, crossing the early convergence line along the eastern coast of Melville Island (East Island), where the tallest updraft was located, are drawn perpendicular to the coast every 15 min (Fig. 8). For the congestus phase, the convergence lines are built along the coasts, where the sea breeze meets the buoyant air masses at the islands' surface. Above these lines, the cumulus congestus formed at the top of the PBL and extended up to the freezing level (e.g., at 6 km west of the coast at 1130 LST and at 15 km at 1200 LST). They produced rain and cold pools (at 8 km west of the coast at 1145 LST and at 15 km west at 1215 LST) that pushed the convergence lines farther inland.

At 1215 LST, the deep convection phase began. The convergence lines, still parallel to the coastlines, were advected toward the islands' center by the sea-breeze surface circulation (Fig. 7d). Few cold pools, shaded in blue in Fig. 7c, contributed to the inland advection of the convergence lines, and to their reinforcement, in the east of Melville Island and in the south of Bathurst Island. The moisture-flux horizontal convergence increased to 5 $g m^{-3} min^{-1}$ in most of the convergence lines. In the east of Melville Island and between the two islands, the two tallest updrafts reached 14-km altitude. The position of these updrafts at 10-km altitude was shifted by 4 km eastward compared to the closest convergence line. This shift in space was due to the delay between the time needed for deep convection to transport near-surface air to this altitude and the time spent by the convergence line to be advected farther inland. One of the two tallest updrafts in the east of Melville Island is shown in Figs. 9a and 9d. Its base was thin (a few hundred meters), and the updraft became larger with altitude (up to 2–3 km). Its top was collocated with the top of the corresponding cloud and was surrounded by an intense subsiding shell, with downward wind stronger than 5 $m s^{-1}$. Such a subsiding shell may have a strong influence on the interaction between the developing cloud and its environment by controlling the entrainment of humid air at the cloud top and sides.

At 1315 LST, the very deep convection phase started. The convergence lines (Fig. 7f) stopped being parallel to the coasts; they were then driven by the edges of the cold pools (Fig. 7e). Whereas some of the convergence lines started to be expelled out of the islands, some others continued to move toward the center of the islands (Fig. 7f), where they intersected with moisture flux horizontal convergence larger than 7 $g m^{-3} min^{-1}$. Above these lines, the two tallest updrafts developed up to almost 18-km altitude, one being located in east-central Melville Island and the other to the west of this island (shown in Figs. 9b,e). At the surface and at $x = 12$ km in Fig. 9b, the latter produced heavy rain, with more than 2 $g kg^{-1}$ in the lowest 3 km. Its base at 3-km altitude was about 3 km across, and it was around 8 km large in the free troposphere, from 6-km altitude up to the TTL base at 14-km altitude. Its top reached the tropopause above 17 km, and the corresponding cloud overshot into the stratosphere. Intense subsiding shells were still present near the top of the tallest updraft, with downward wind stronger than 10 $m s^{-1}$, and along the edges of the tallest updraft, between 8- and 13-km altitudes. These intense downward motions occurred at the cloud edges, changing the properties of the entrained air from dry to humid. The other updraft shown in Figs. 9b and 9e, at $x = 22$ km, also produced heavy rain and had a large base, but its vertical development was inhibited by the subsiding air that detrained from the tallest updraft.

At 1415 LST, the mature convection phase began. The updrafts led by the intersection of the convergence lines at the island center gathered and connected with each other to form convective clusters (Fig. 7h). The tallest one is shown in Figs. 9c and 9f. The convective clusters

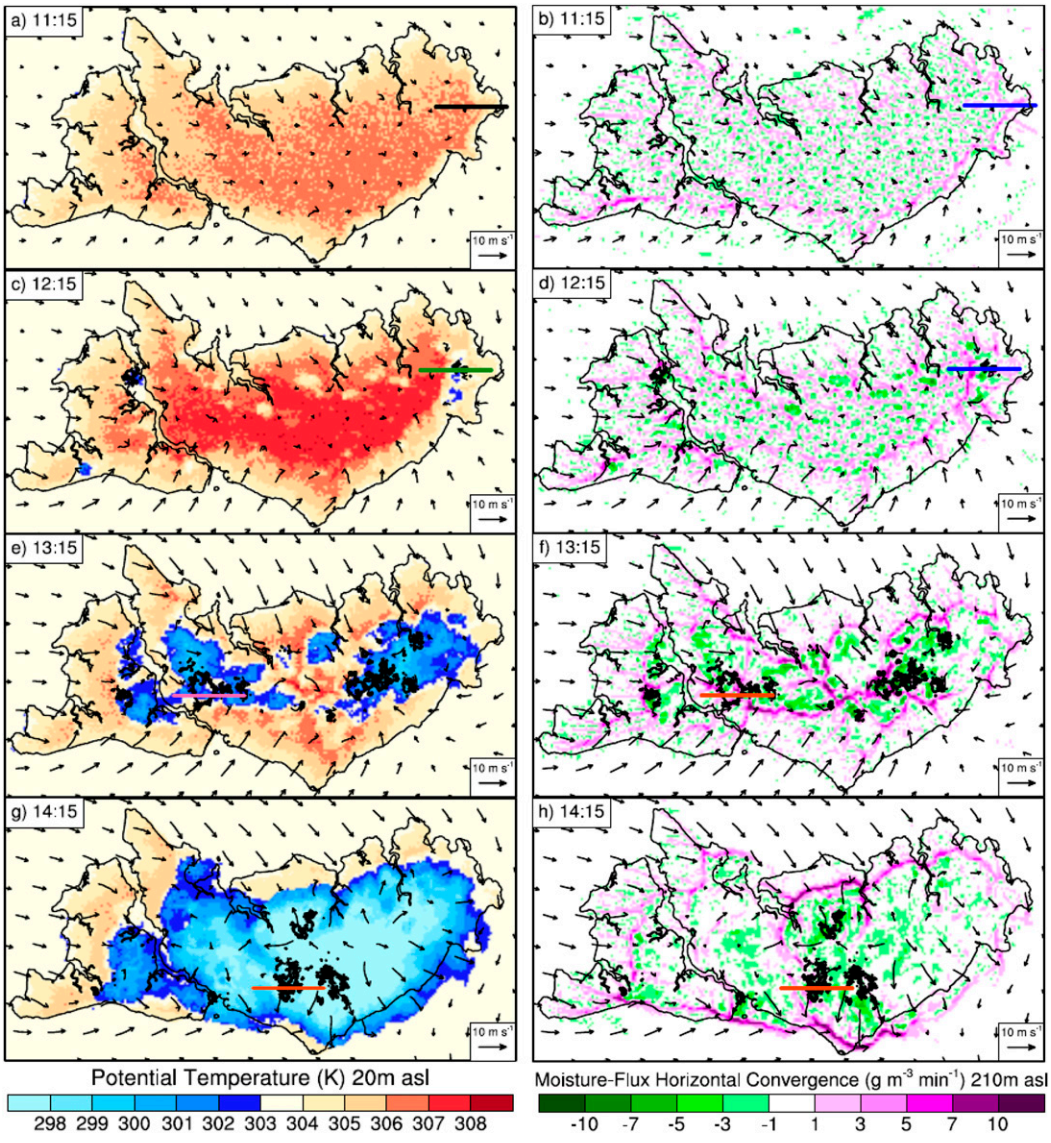

FIG. 7. (a),(c),(e),(g) Horizontal cross sections of potential temperature at the first model level, 20 m above the surface. (b),(d),(f),(h) Horizontal cross sections of moisture flux horizontal convergence 210 m above the surface level. The horizontal wind is superimposed. (top)–(bottom) The congestus (1115 LST), deep (1215 LST), very deep (1315 LST), and mature (1415 LST) convection phases are represented. The black contours show the location of the updrafts at 10-km altitude. The colored straight lines indicate the positions of the vertical cross sections presented in Figs. 8 and 9.

generated heavy loads of rain below their bases. This led to a massive cold pool (Fig. 7g) that spread horizontally, with near-surface potential temperature down to less than 298 K (6 K less than outside the cold pool) and humidity divergence larger than $3\,g\,m^{-3}\,min^{-1}$ over the center of the islands. This massive cold pool expelled the convergence lines out of the islands. The base of the convective cluster, between 4- and 6-km altitude, was multiple (Fig. 9c). Although it formed a connected structure extending more than 7 km horizontally, its shape was more complex than the very deep updraft in Fig. 9b. The top of the convective cluster was at 13-km altitude. Intense subsiding shells were no longer located at the cloud top only but were ubiquitous around the updrafts. Subsiding shells stronger than $5\,m\,s^{-1}$ were found between 7- and 16-km altitudes. The overall structure of the vertical wind inside the cloud system appeared much more complex than for the deep and very deep convection phases, with variations of vertical velocities larger than $2\,m\,s^{-1}$ that spread in the whole cloud system. The cloud showed a large anvil in the upper troposphere, between 11- and 15-km altitude,

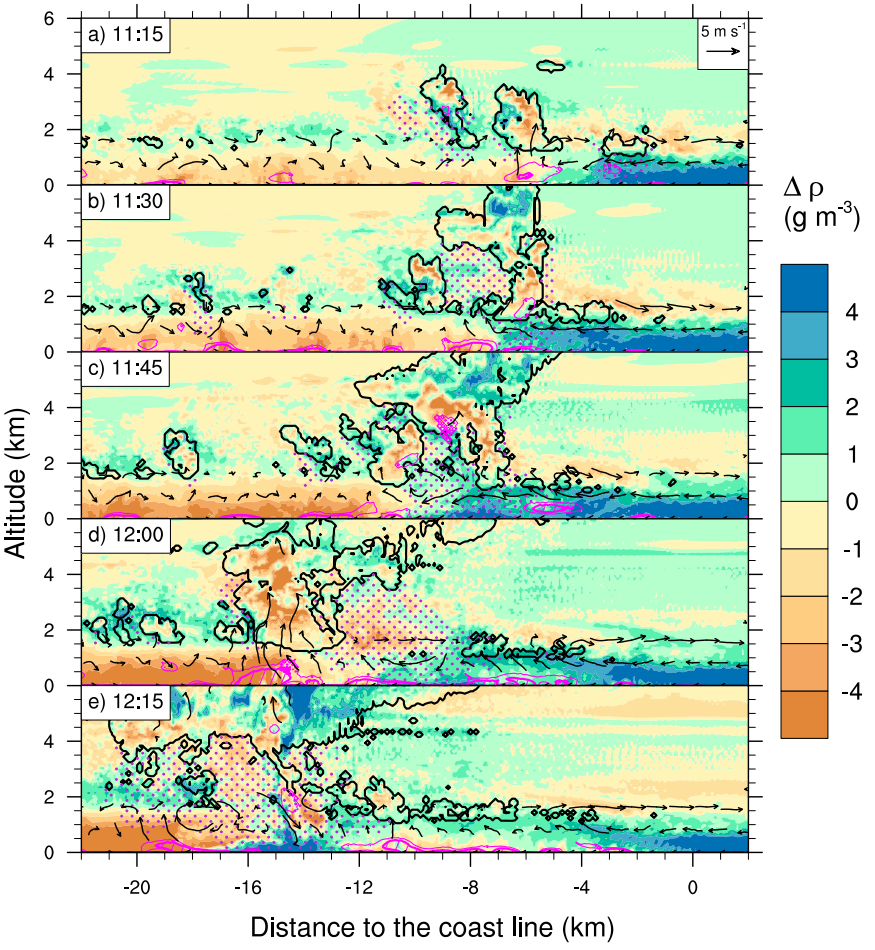

FIG. 8. Vertical sections, located across the blue line in Fig. 7 at 1115 LST, of density anomaly (color shading), zonal and vertical wind (arrows), cloud envelope (black contour at 5 mg kg^{-1}), rain mixing ratio over 10 mg kg^{-1} outside the clouds (dots), and moisture flux horizontal convergence over 3 and 5 g m^{-3} min^{-1} (magenta contours) at (a) 1115, (b) 1130, (c) 1145, (d) 1200, and (e) 1215 LST.

with an upper portion stretched by the easterlies between the tropopause and 18-km altitude (Fig. 9c).

To analyze the environment in which the tallest updrafts developed, the vertical profiles of moisture flux horizontal convergence, equivalent potential temperature θ_e, and water content were averaged inside cylinders centered over these updrafts, 15 min before their occurrence (Fig. 10). The radius of the cylinders was 8 km so as to entirely encompass the volume later occupied by the updrafts and their close environment. At 1300 LST, before the triggering of the very deep convection phase, θ_e at the surface was 356 K (the same value as at 1200 LST), and the CAPE, 2146 J kg^{-1}, was very close to the 1200 LST value. The moisture flux horizontal convergence doubled (1.6 vs 0.7 g m^{-3} min^{-1}) because of the intensification of the convergence lines discussed above. The hydrometeor content in the lower troposphere, up to 9-km altitude, also doubled in value compared to 1200 LST, with the cloud development of the deep convection. This gave an extra latent heat release when the liquid hydrometeors were entrained inside the updraft and frozen during their uplift. The water vapor content increased nonuniformly, with local increase around 1 g kg^{-1}. The intensification of the convergence lines, the loading of the low troposphere with liquid hydrometeors, and the increase of humidity in the low troposphere may explain why the tallest updrafts reached the stratosphere after 1300 LST and not before. At 1400 LST, the liquid hydrometeor content had doubled again in comparison to 1300 LST (2 g kg^{-1} on average between 3 and 4.5 km), whereas the icy hydrometeor content ranged from 2 to 4 g kg^{-1} between 5 and 15 km. These heavy loads of ice in the troposphere did not favor the growth of the updrafts to

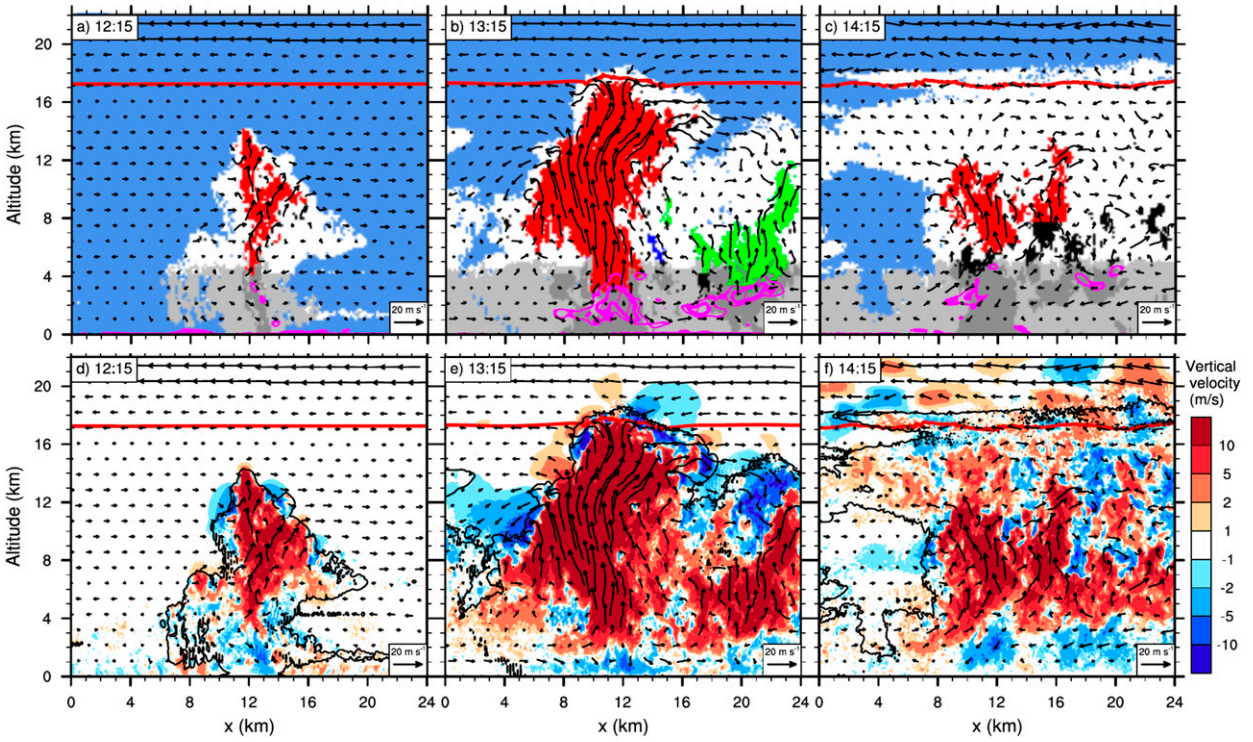

FIG. 9. Vertical cross sections of one of the two tallest updrafts at the (a),(d) deep, (b),(e) very deep, and (c),(f) mature convection phases in the LES. (a)–(c) The tallest updraft is in red; the other updrafts are in bright colors or black. Clear sky is in blue, cloud with cloud content larger than 10 mg kg^{-1} is in white, rain heavier than 10 mg kg^{-1} is in gray, and rain heavier than 2 g kg^{-1} is in dark gray. The magenta contours indicate areas of moisture flux horizontal convergence over 3 and 5 g m^{-3} min^{-1}. (d)–(f) The vertical wind speed is shaded, and the cloud and rain content larger than 10 mg kg^{-1} are contoured in black. The tropopause is represented by a red line.

the stratosphere, since entrained ice particles only made a negative contribution to the buoyancy. In contrast, they could contribute to downdraft development, especially when downdrafts reached the freezing level and icy hydrometeors melted, absorbing latent heat. The water vapor content continued to increase nonuniformly, still with amplitudes around 1 g kg^{-1}. The main reason why the tallest updrafts grew less high during mature convection than during very deep convection could be found in the significant reduction of surface θ_e (−2.5 K on average). This reduction was because of massive cold pools reaching the surface, as can be seen in Fig. 7g, and the subsequent decrease of the CAPE value, here by a factor 2.

The tallest updrafts, and convection in general, appeared above the convergence lines that were first driven by the sea-breeze surface circulation only, and then together with the downdrafts produced by the previous convection [in agreement with Saito et al. (2001)'s analysis]. The humidity convergence at the surface increased and peaked when the convergence lines intersected over the islands' center. At this time (the very deep convection phase), the tallest updrafts had large bases and were supplied with surface air with large θ_e. They grew in an environment moistened by the previous deep convection and reached the stratosphere. Intense subsiding shells at the cloud top and sides may control the local interactions between the tallest updrafts and their environment. Later (during the mature convection phase), the cold pools replaced the warm buoyant air at the surface with colder air: the tallest updrafts no longer reached the stratosphere.

b. *Properties*

The geometrical, dynamical, thermodynamical, and microphysical properties of the tallest updrafts in the deep, very deep, and mature convection phases are examined (Fig. 11). The geometry of the tallest updrafts is described using the vertical profile of the effective width in Fig. 11a. In the deep convection phase, the tallest updraft was 10 km tall and started at 4-km altitude. In the very deep convection phase, the tallest updraft was a convective plume that reached the lower stratosphere. Of the three phases, the very deep convection one presented the tallest updraft with the largest vertical extent (16 km), maximal effective width (more than 8 km between 8- and 12-km altitudes),

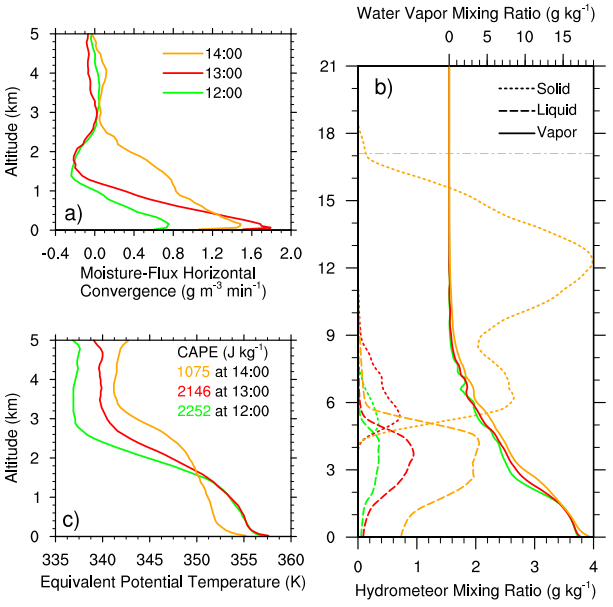

FIG. 10. Vertical profiles of (a) moisture flux horizontal convergence, (b) water mixing ratio, and (c) equivalent potential temperature, averaged in a cylinder of 8-km radius and centered at the location of the tallest updrafts shown in Fig. 9 but taken 15 min earlier than times shown in Fig. 9. The profiles preceding the deep, the very deep, and the mature convection phases at 1200, 1300, and 1400 LST, are in green, red, and orange, respectively. In (b), water vapor mixing ratio is in solid lines, the sum of the liquid species in dashed lines, and the sum of the solid species in dotted lines. The tropopause is located with a dashed–dotted line in (b). The CAPE at the surface, computed from pressure and temperature fields averaged inside the cylinders, is indicated for 1200, 1300, and 1400 LST in (c).

and effective width of the base (more than 4 km). In the mature convection phase, the tallest updraft was the convective cluster shown in Fig. 9c. Its vertical and horizontal extents, 13 and 7 km respectively, were lower than those of the tallest updraft of the very deep convection phase.

Concerning the dynamical properties, vertical profiles of the average and maximal vertical velocities of the tallest updrafts are shown in Fig. 11b. For the tallest updrafts of the deep convection and the mature convection phases, the vertical velocity was almost constant with altitude, with an average value between 14 and 16 m s^{-1} and a maximum value between 25 and 35 m s^{-1}. For the very deep convection phase, the average vertical velocity was much greater, increasing from 15 m s^{-1} at 4-km altitude to 22 m s^{-1} at 10-km altitude, and then decreasing, back to 17 m s^{-1} in the TTL between altitudes of 14 and 17 km. The maximal vertical velocity was also larger for the very deep convection phase than for the other two phases: over 45 m s^{-1} between 7- and 14-km altitude, and over 33 m s^{-1} in the TTL.

The positive buoyancy of the tallest updrafts (Fig. 11c) explains the large vertical velocities reported above. To quantify the negative contribution of the hydrometeor loading (Fig. 11d), the buoyancy computed without taking into account the hydrometeor loading is also shown in Fig. 11c. The tallest updrafts showed positive values of buoyancy (around 0.1 m s^{-2}) up to their level of neutral buoyancy, between 10- and 13-km altitudes. As a consequence, they exhibited upward vertical velocities up to at least 3 km above their level of neutral buoyancy within the stratified TTL. The hydrometeor loading was around 8 g kg^{-1}, which acts to reduce the buoyancy by a factor of 2. Note that at the freezing level (around 5 km), the liquid hydrometeor contents decreased sharply with height because of fast heterogeneous freezing of rain drops, but supercooled water remained up to 8-km altitude, as a result of more gradual homogeneous freezing of the cloud droplets. The tallest updraft of very deep convection presents outstanding properties. It extended even 5 km above its level of neutral buoyancy and exhibited the largest values of buoyancy and hydrometeor loading, up to 11 g kg^{-1}, and larger than 6 g kg^{-1} up to the tropopause.

The upward transport of near-surface warm, moist air parcels is a source of buoyancy in the tallest updrafts. This process is examined using the profiles of the frozen moist static energy (MSE$_i$) of the tallest updrafts compared to the environment (Fig. 11e). The environmental profile was taken from the large-scale oceanic environment, shown in Fig. 2. MSE$_i$ is conserved when an air parcel exchanges no mass with its surrounding, even if its water content changes phase. Whatever the convection phases, the average MSE$_i$ is almost constant with height in some large parts of the updrafts, suggesting little dilution there. Because the average MSE$_i$ was larger than in the environment up to their level of neutral buoyancy, a large proportion of the buoyant air found in the tallest updrafts was likely transported with weak dilution from the islands' surface, where it was heated by the intense heat fluxes (Figs. 5c, 10c). The average MSE$_i$, however, decreased with height at the updraft base. Further, the maximal values of MSE$_i$ differed from the average ones, up to 10 K for the very deep convection phase. This indicates that dilution occurred within the tallest updrafts.

The latent heat release due to water condensation, freezing, and deposition is the other source of buoyancy. In the absence of any dilution, the potential temperature θ can increase only because of the latent heat release. To investigate the latent heat release inside the tallest updrafts, their lapse rate, computed as the vertical gradient of their average potential temperature, is shown and compared to the environmental lapse rate (Fig. 11f). In the absence of any latent heat release, the lapse rate in the updrafts ranges from zero without any mixing to the

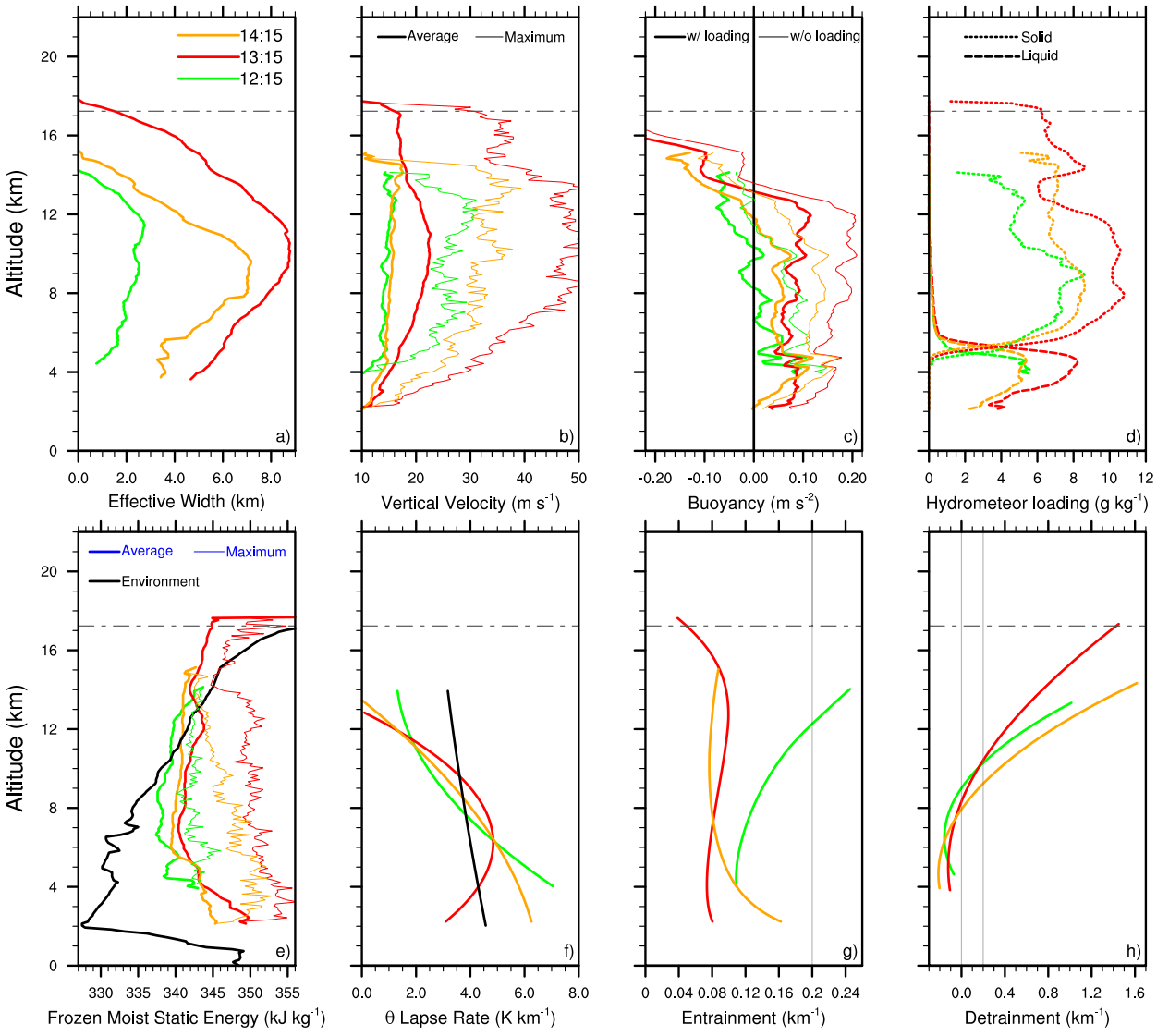

FIG. 11. Vertical profiles of (a) effective width, (b) vertical velocity, (c) buoyancy, (d) hydrometeor loading, (e) frozen moist static energy, (f) θ lapse rate, (g) entrainment, and (h) detrainment for one of the two tallest updrafts of the deep convection (1215 LST; green), very deep convection (1315 LST; red), and mature convection (1415 LST; orange) phases. In (b) and (e), thick lines stand for average values and thin lines for maximum values. In (c), thick lines stand for the total buoyancy and thin lines for the buoyancy computed without taking into account the hydrometeor loading. In (d), the solid phase is represented by dotted lines and the liquid phase by dashed lines. In (e) and (f), the environment profile is in black. In (g) and (h), vertical straight lines indicate 0 and 0.2-km^{-1} values for comparison. The tropopause is represented by a gray dashed–dotted line.

environmental lapse rate in case of complete mixing. Beyond, a larger lapse rate inside the updraft than in the environment necessarily implies some latent heat release. As a result, the updraft lapse rate was larger than the environmental one up to 8–10 km, regardless of the convection phases. This shows that the latent heat release contributed to their positive buoyancy. The largest and highest overtaking was found inside the tallest updraft of very deep convection, between 7 and 10 km, consistent with its largest buoyancy. The role of the latent heat release needs to be further investigated and quantified.

The entrainment of environmental air by the tallest updrafts (Fig. 11g) was computed considering that the total water content was conserved when no dilution occurred. The loss of water due to precipitation was neglected. The underlying assumption is that the local budget of the falling in and falling out precipitation is small compared to the change of total water content due to dilution. To compute entrainment rates ε that were

comparable with the entrainment of the subgrid updrafts parameterized in the deep convection schemes, we used the bulk formula $dq_u/dz = \varepsilon(q_e - q_u)$, where the environmental profile of total water content q_e corresponds to the large-scale environment. Note that ε is subject to uncertainties relative to the conservative variable selected. It was calculated using MSE_i up to 6–8 km (below the altitude of the MSE_i minimum). Values on the same order as those derived from the total water content were obtained. Concerning the oceanic large-scale environment, it was assumed not to vary during the course of the simulation, so the initial profile shown in Fig. 2 was used for q_e. The vertical profiles of the averaged total water content in the updrafts q_u and the environmental profile were fitted in order to avoid large variations of entrainment with altitude.

The entrainment values of the tallest updrafts were low, on the order of 0.1 km^{-1} (Fig. 11g). Such a low value was found for the least entraining plume of oceanic tropical clouds up to 7 km (de Rooy et al. 2013) and of Amazonian deep convection up to 14 km (Khairoutdinov and Randall 2006). The tallest updraft of the deep convection phase showed larger values in the upper troposphere, over 0.2 km^{-1} above 12 km, in the range of typical entrainment rate found by Del Genio and Wu (2010). In contrast, the profile of entrainment of the very deep and mature convection phases was low even in the upper troposphere. The surrounding cloud may have had a buffering effect, as the tallest updrafts did not entrain air from the environment but rather cloudy air from the previous convection phase (see the water content 15 min earlier in Fig. 10b). Remarkably, the tallest updraft of the very deep convection phase exhibited an almost uniform entrainment of 0.08 km^{-1} between 2 and 18 km. It appeared then to be part of the least entraining updrafts up to the tropopause evidenced so far.

The capability of the tallest updrafts to redistribute air parcels at upper levels is illustrated with their detrainment δ (Fig. 11h). The detrainment is computed from the budget of the conservative variable used for the entrainment ε, leading to the expression $dM/dz = (\varepsilon - \delta)M$, where M is the vertical mass flux of the tallest updraft. Whatever the convection phases, the tallest updrafts showed detrainment values exceeding 0.4 km^{-1} above 12 km, strongly increasing with the altitude up to around 20 times the values of the entrainment rate. Much larger detrainment rates than entrainment rates were already found by de Rooy and Siebesma (2008). Note that the tallest updraft of very deep convection redistributed air parcels up to the tropopause. This was at a much higher altitude than the ones of the two other convection phases, and this was directly linked with its larger vertical extent. At lower levels (from the base to 8-km altitude), the detrainment was slightly negative. These negative values noticed in previous studies (e.g., de Rooy and Siebesma 2010) are unphysical and usually cut off to zero. This is a limitation of the bulk model, which is due to the humidity of the air entrained into the tallest uprafts, larger than the bulk model for entrainment would assume.

Among the intense convection phases, the very deep convection phase stands out, with the tallest updrafts having exceptional dimensions (16 km tall and over 8 km wide), vertical velocities (over 15 $m\,s^{-1}$ on average and over 30 $m\,s^{-1}$ as the maximum), buoyancy (up to about 0.1 $m\,s^{-2}$), water loading (over 6 $g\,kg^{-1}$ throughout the TTL), and extremely low entrainment (0.08 km^{-1}) up to the tropopause. The following section investigates the entrainment and the mass transport in these tallest updrafts in greater detail.

c. *Mass and water transport*

To analyze the capacity of the tallest updrafts to carry water and surface air masses up into the stratosphere, the vertical profiles of the air mass flux and the water mass flux are shown for the tallest updrafts at 1315 LST in Figs. 12a and 12b, respectively. The question of the dilution of the tallest updrafts with the environmental air was addressed with vertical cross sections of MSE_i, of turbulent kinetic energy (TKE), and of two low-troposphere passive tracers (Fig. 13). The origin of the air inside the tallest updrafts was quantified with five different passive tracers (Fig. 14).

The vertical profiles of the air mass flux and water mass flux were computed at 1315 LST, considering all the updrafts, the two tallest and the tallest one only (Figs. 12a,b). The air mass flux of 10^7 $kg\,s^{-1}$ for all the updrafts at 17-km altitude, considering the area of the domain of simulation (5×10^{10} m^2), exactly matched the value of 2×10^{-4} $kg\,m^{-2}\,s^{-1}$ found by Chaboureau et al. (2007). They averaged the flux as a result of around 50 overshoots over 24 h, which is equivalent to the two tallest updrafts' contribution for the hour of very deep convection in our simulation. As already seen in section 3b at two specific altitudes, the two tallest updrafts accounted for a large proportion of the air mass and water mass fluxes because of all the updrafts (Figs. 12a,b). They were in the range of 15%–50% between 2- and 5-km altitudes, and 50%–80% between 5- and 11-km altitudes, where their contributions to the air and water mass fluxes were up to 10^9 and 10^7 $kg\,s^{-1}$, respectively. Aloft, the mass fluxes decreased sharply with altitude, but the contribution of the two tallest updrafts continued to increase, reaching 100% at 16-km altitude and above.

To investigate the dilution of the tallest updrafts by the environmental air, Fig. 13a represents MSE_i for the tallest updraft at 1315 LST in the same cross section as in

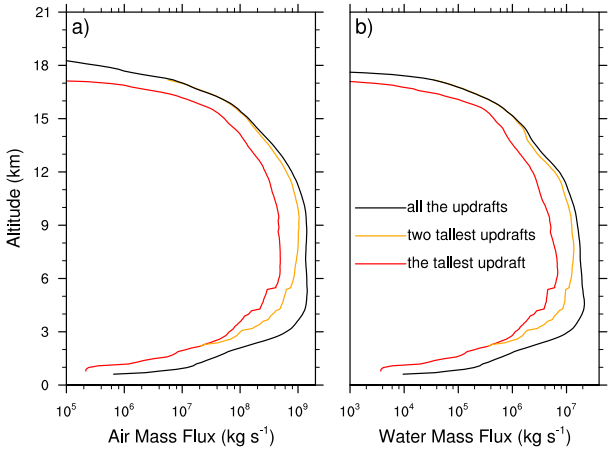

FIG. 12. Vertical profiles of (a) vertical air mass flux and (b) vertical water mass flux at 1315 LST in the LES. The contribution of the tallest updraft, the two tallest updrafts, and all the updrafts are in red, orange, and black, respectively.

Fig. 9. The air in the large base of this updraft had the same values of MSE_i (around 349 kJ kg^{-1}) as the air in the PBL. It was transported up to the freezing level (around 5-km altitude) with almost no dilution. Between 5- and 13-km altitudes, the updraft exhibited a core with MSE_i about 345–348 kJ kg^{-1}, and some other parts with lower MSE_i (335–345 kJ kg^{-1}), indicating mixing with the environmental air. Between 14- and 17-km altitudes (in the TTL), MSE_i in the updraft was slightly lower than below, indicating that a larger amount of tropospheric air had been entrained. In the TTL, the environment showed larger MSE_i than in the updraft. Detrainment outside the updraft became apparent, with, for example, $MSE_i = 342$ kJ kg^{-1} between $x = 14$ and 18 km and $z = 15$ and 17.5 km.

The mixing is further investigated with TKE shown in the same vertical cross section (Fig. 13b). The subcloud turbulent eddies that contribute to the mixing of environmental air inside the updrafts are assumed to have a typical length smaller than 1 km. TKE was then calculated as the subgrid-scale TKE plus the grid-scale turbulent kinetic energy. The latter was computed using the departure of the three components of the resolved wind field from their average values over a 900-m square. TKE values in the cloud ranged between 1 and 70 m^2 s^{-2}. Interestingly, at the base of the updraft, around 4-km altitude, only the borders of the updraft showed intense mixing by turbulent eddies activity (TKE around 20 m^2 s^{-2}). In contrast, the core showed lower TKE values, between 1 and 10 m^2 s^{-2}, while the wind speed was very high, over 20 m s^{-1} upward. The ascent in the lowest part of the updraft was thus less turbulent in the core than at the edges, reducing the dilution of the surface air masses transported in the core. Aloft, and up to the tropopause, mixing was intense at the edge of the updraft and also inside it, at the edge of the core. The inhomogeneous composition of the updraft, already seen with MSE_i in Fig. 13a, corresponded to the inhomogeneous mixing occurring in regions of strong gradient of MSE_i. Also, an intense mixing due to subcloud turbulent eddies occurred in the regions of strong detrainment, between 13- and 18-km altitudes.

Passive tracers are now shown on the same vertical cross section to visualize the entrainment of air from different layers into this updraft (Figs. 13c,d). Five tracers were initialized with a concentration value of 1, 15 min earlier (at 1300 LST) in the PBL (PBL tracer), between the PBL top and the freezing level (low-troposphere tracer), between the freezing level and 16-km altitude (upper-tropospheric tracer), between 16- and 17-km altitudes (TTL tracer), and above 17-km altitude (stratosphere tracer). The PBL tracer (Fig. 13c) was efficiently uplifted by the updraft. Concentrations found in the updraft core were as high as 0.9 up to 9-km altitude, 0.8 up to 12-km altitude, and 0.3 up to 17-km altitude, the usual level of the tropopause. Consistently, concentrations of 0.3 of a subcloud tracer have been found in the uppermost 2 km of the troposphere for oceanic deep convection in radiative–convective equilibrium (Romps and Kuang 2010). In the tallest updraft, the dilution of the PBL air was mostly due to the entrainment of environmental air below the freezing level, materialized by the low-troposphere tracer (Fig. 13d), and especially around the base of the updraft.

The distributions of the different origin layers for the air masses inside the tallest updrafts are further quantified in Fig. 14. The tallest updraft of the deep convective phase (Fig. 14a) was composed of 40% of PBL air at its base and about 20% at its top. Up to 10-km altitude, half of its volume was composed by air entrained below the freezing level. Above 10-km altitude, it was mostly composed of upper-tropospheric air. This result is consistent with the larger values of entrainment in the upper troposphere shown in Fig. 11g. The tallest updraft of the very deep convective phase (Fig. 14b) contained more than 65% of PBL air in its base and about 25% in its top. Whatever the levels in this updraft, the PBL air made up more than 20% of the air. This indicates a weak dilution of the updraft by the environmental free-tropospheric air. The tallest updraft of the mature convection phase (convective cluster; Fig. 14c) was made of about 40% of PBL at its base, down to 0% in the last 2 km at its top. Whatever the altitude, the air from the lower free troposphere composed about 60% of the convective cluster volume. This is consistent with the relatively large values of entrainment in the lower troposphere shown in Fig. 11g. The entrainment of low-MSE_i air between the

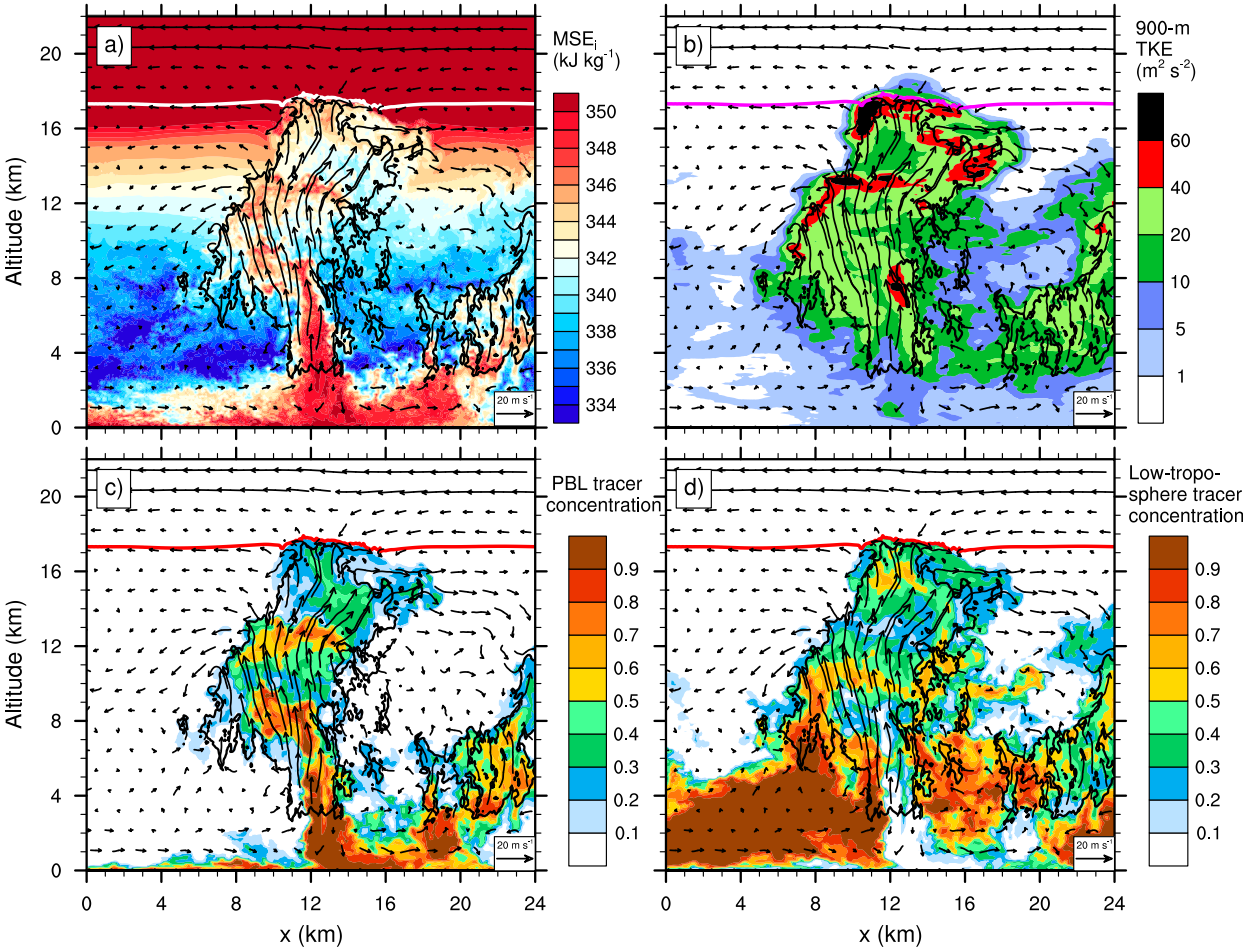

FIG. 13. Vertical cross sections of the second tallest updraft at 1315 LST: (a) frozen moist static energy, (b) turbulent kinetic energy, and tracers initialized 15 min earlier (c) in the PBL and (d) between the PBL top and the freezing level.

PBL and the freezing level partly explains the MSE$_i$ values in the convective cluster (Fig. 11e), which were lower than in the tallest updraft of the very deep convective phase. In the upper troposphere, the entrainment by the convective cluster was reduced (Fig. 11g), whereas almost no PBL air was left at the top of the updraft (Fig. 14c). This apparent paradox may be explained by the fact that the entrainment was computed using the total water as a conservative quantity and that the air entrained by the convective cluster was loaded with hydrometeors (Fig. 10b). The little change in the water loading of the convective cluster with altitude (low entrainment in Fig. 11g) may then hide its dilution by the free-tropospheric air with low MSE$_i$ (Fig. 14c).

During the very deep convection phase, the two tallest updrafts accounted for most of the air mass flux and the water mass flux from the freezing level up to the stratosphere. Most of the entrained air came from the lower troposphere, below the freezing level. It was transported at the edges of the tallest updrafts and only mixed with the core several kilometers away from its source region. The exceptional buoyancy of the tallest updrafts is explained by a transport without dilution, especially in the core of the updraft base, where a less-turbulent vertical ascent was seen. The large amount of water transported above the freezing level also led to a large additional gain in buoyancy by latent heat release.

5. Conclusions

The giga-LES (100-m grid spacing) of Hector the Convector on 30 November 2005 performed by Dauhut et al. (2015) was used to investigate the organization of the vertical mass fluxes up to the stratosphere. By applying a clustering algorithm, the updrafts were identified as connected individual 3D structures, where the vertical velocity exceeded 10 m s^{-1}. Among the thousands of updrafts detected at any time when the convection was

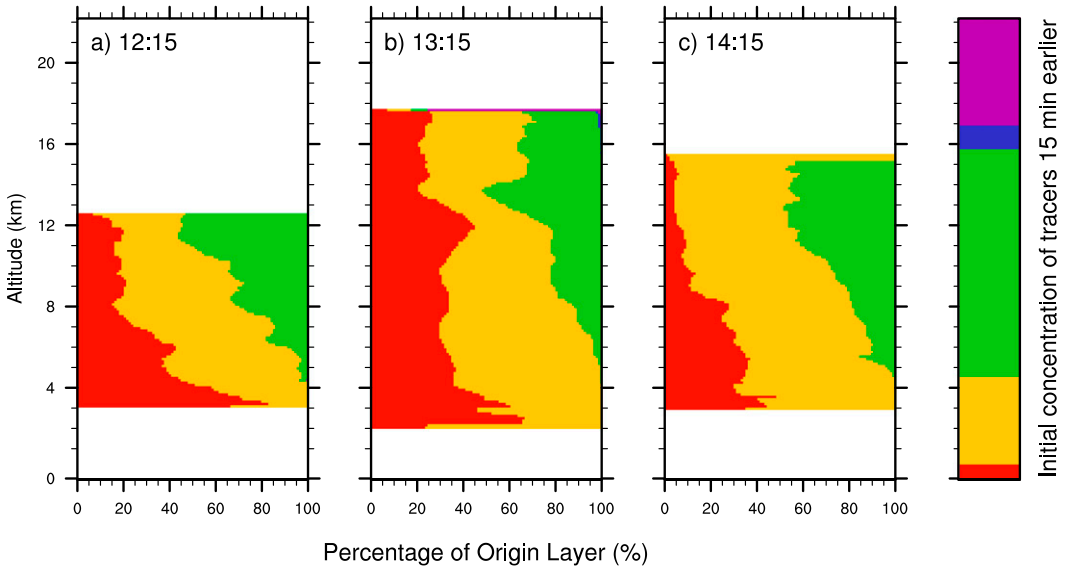

FIG. 14. Distribution of the passive tracers inside the tallest updrafts at (a) 1215, (b) 1315, and (c) 1415 LST. The passive tracers were initialized 15 min earlier in the following layers: the PBL (red), the lower troposphere (yellow), the upper troposphere (green), the TTL (dark blue), and the stratosphere (purple).

deep, only a dozen were more than 4 km tall, and the two tallest were the most important coherent structures for the transport toward the stratosphere. Their contribution to the air mass flux and water mass flux was over 50% above the freezing level and over 90% across the TTL.

The key processes that enabled Hector and its two tallest updrafts to reach the stratosphere have been highlighted. They are schematically depicted in Fig. 15 during the four convective phases (congestus, deep, very deep, and mature convection):

1) The sea breeze: It leads to the mesoscale convergence of the surface winds, enhances the convergence of the humidity above the islands, and triggers the first congestus clouds and precipitation along the coast. The sea breeze lasts throughout the development of Hector.
2) The cold pools: They are generated by the downdrafts of the precipitating cumulus, and they lift the air that has been warmed at the surface of the islands. They trigger new precipitating cumulus at their edge. From the mature convection phase onward, the massive cold pools prevent warm, moist air from being supplied to the upcoming updrafts.
3) The convergence lines: They are first built up by the sea-breeze fronts and then intensified by the cold pools. They determine where the tallest updrafts appear. The cold pools also push the convergence lines inland, where the convergence lines are supplied with warm, moist air and eventually intersect each other, leading to extended areas of large convergence of humidity.
4) The low dilution of the updrafts: The dilution of the tallest updrafts is found to be particularly low during the very deep convection phase. This is in marked contrast with the deep convection phase, during which the entrainment of environmental air is greater, and with the mature convection phase, during which low-MSE_i air of the low troposphere is entrained.

The tallest updrafts appear above the convergence lines. During the very deep convection phase, the tallest updrafts show their maximal values of effective width (8 km in midtroposphere), buoyancy (up to $0.1\,m\,s^{-2}$), vertical velocities (up to $50\,m\,s^{-1}$), and hydrometeor contents ($10\,g\,kg^{-1}$). The weakly diluted ascent in the base of the tallest updrafts leads to the uplift of a large load of liquid water above the freezing level, contributing to the great buoyancy of the tallest updrafts. The outstanding strength of these tallest updrafts makes them akin to the hot towers postulated by Riehl and Malkus (1958). However, they are subject to uncertainties in their microphysical representation. This was documented recently in two model intercomparisons for precipitating shallow convection (van Zanten et al. 2011) and deep convection (Varble et al. 2014). In the latter study, the models produced too-strong updrafts that transported too much rain through the freezing level. The subsequent large freezing leads to large latent heat release, positive buoyancy, and eventually too-efficient

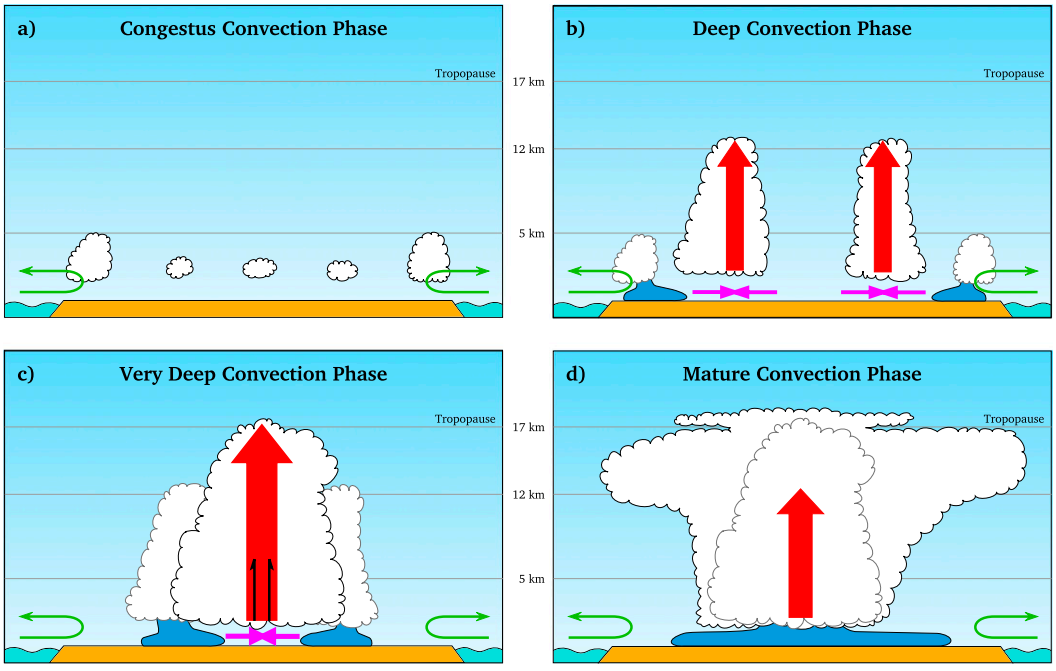

FIG. 15. Schematic diagram of the successive phases of convection, emphasizing the processes that lead the thunderstorm to overshoot into the stratosphere. (a) The congestus convection phase, (b) the deep convection phase, (c) the very deep convection phase, and (d) the mature convection phase are illustrated. The freezing level at 5 km, the level of the deep convective outflow at 12 km, and the cold-point tropopause at 17 km are represented by the gray solid lines. The sea breeze (thin green arrows) forces convergence above the idealized island. The main cumulus clouds of the current phase and of the previous phase are outlined in black and gray, respectively. The cold pools (blue) force and intensify the moisture flux horizontal convergence (magenta) that leads to the growth of the tallest updrafts (thick red arrow). The low values of dilution by entrainment of the environmental air are illustrated by two embedded black half arrows.

transport of water. This positive feedback (too-strong updrafts are likely to become even stronger) may explain why the models diverge from the observed in-cloud vertical velocities. Other studies (Lebo et al. 2012; Grabowski and Jarecka 2015) discussed the impact in convection of the saturation adjustment, an assumption common to many bulk microphysics schemes. The latter leads to boost the updrafts just aloft the freezing level, rather than in a wider range of altitudes within the upper troposphere.

The large width of the tallest updrafts, even at the base (about 4 km), also helps to keep the dilution low. Below the freezing level, the entrained air is mixed with only the outer part of the tallest updrafts, whereas their core is kept weakly diluted. The large widths of the tallest updrafts and the mixing confined at their outer edges are consistent with the weak effective entrainment. It would be interesting to investigate the mixing with further details, especially since the most energetic motions are resolved in this giga-LES. Some tracer methods allow one to compute the local entrainment by the eddies at the interface between the updrafts and their environment. For example, the impact of the intense subsiding shells shown by Glenn and Krueger (2014) and evidenced here may be estimated. Their role in inhibiting or favoring the exchanges between the tallest updrafts and their close environment—including the potential interaction and aggregation between the updrafts—remains to be documented indeed. This will be investigated in an upcoming isentropic analysis dedicated to the overturning circulation of Hector the Convector.

The overshoots into the stratosphere appear during the very deep convection phase. During this phase, a large flux of PBL air mass crosses the whole TTL. Afterward, the remnants of clouds that spread in the stratosphere are a signature of the cross-tropopause transport. An aspect not yet studied in this LES is the sequence of mechanisms leading to the irreversibility of the transport into the stratosphere. A forthcoming study will analyze the mixing processes of the tropospheric air mass in the stratosphere.

Finally, it would be worthwhile to compare the internal organization of other cases of very deep convection with the one described in this study. Are the four

processes mentioned above common to the other tropical storms that overshoot the stratosphere? The sea breeze is absent for most of the African and South American cases since they are generally purely continental. Mesoscale circulations, instead of sea breeze, can trigger congestus convection, however. Cold pools are already known to play a key role in the organization and the deepening of the convection [e.g., Schlemmer and Hohenegger (2014) and the references therein]. Intense convergence lines at the edges of the cold pools have also been evidenced, but their intersection as a systematic triggering factor of the deepest convection still needs to be proved. The existence of very tall updrafts, accounting for most of the transport, and their extremely low dilution, are challenging to observe. Their ubiquity in very deep convection is even more difficult to demonstrate. Field campaigns to investigate the deep interior of the tallest thunderstorms, together with associated modeling studies with LESs, would then greatly advance our knowledge of very deep convection, its dynamics, and its capacity to contribute to troposphere-to-stratosphere transport. Further, the very tall updrafts should be represented by the convection parameterization scheme of climate models. This is not the case, as the contribution of very deep convection to the troposphere-to-stratosphere transport is found negligible by existing climate models. Our study pointed out the role of the convergence flux in the boundary layer in triggering and driving the convection, while CAPE kept its initial value during the 1-h-long deep convection phase. Such a process might now be represented in the ECMWF model. Indeed, a recent convective closure subject to boundary layer was shown to improve the representation of equilibrium and nonequilibrium convection (Bechtold et al. 2014). The implementation of low entrainment rate in convective plumes remains to be investigated.

Acknowledgments. This research was supported by the StratoClim project funded by the European Union Seventh Framework Programme under Grant Agreement 603557. Computer resources were allocated by GENCI through Projects 90569 and 100231 (Grand Challenge Turing). We thank the editor and the anonymous referees for their comments, which helped to improve the overall quality of the paper.

REFERENCES

Bechtold, P., N. Semane, P. Lopez, J.-P. Chaboureau, A. Beljaars, and N. Bormann, 2014: Representing equilibrium and nonequilibrium convection in large-scale models. *J. Atmos. Sci.*, **71**, 734–753, doi:10.1175/JAS-D-13-0163.1.

Brunner, D., and Coauthors, 2009: The SCOUT-O3 Darwin Aircraft Campaign: Rationale and meteorology. *Atmos. Chem. Phys.*, **9**, 93–117, doi:10.5194/acp-9-93-2009.

Chaboureau, J.-P., J.-P. Cammas, J. Duron, P. J. Mascart, N. M. Sitnikov, and H.-J. Voessing, 2007: A numerical study of tropical cross-tropopause transport by convective overshoots. *Atmos. Chem. Phys.*, **7**, 1731–1740, doi:10.5194/acp-7-1731-2007.

Chemel, C., M. R. Russo, J. A. Pyle, R. S. Sokhi, and C. Schiller, 2009: Quantifying the imprint of a severe Hector thunderstorm during ACTIVE/SCOUT-O3 onto the water content in the upper troposphere/lower stratosphere. *Mon. Wea. Rev.*, **137**, 2493–2514, doi:10.1175/2008MWR2666.1.

Corti, T., and Coauthors, 2008: Unprecedented evidence for deep convection hydrating the tropical stratosphere. *Geophys. Res. Lett.*, **35**, L10810, doi:10.1029/2008GL033641.

Crook, N. A., 2001: Understanding Hector: The dynamics of island thunderstorms. *Mon. Wea. Rev.*, **129**, 1550–1563, doi:10.1175/1520-0493(2001)129<1550:UHTDOI>2.0.CO;2.

Cuxart, J., P. Bougeault, and J.-L. Redelsperger, 2000: A turbulence scheme allowing for mesoscale and large-eddy simulations. *Quart. J. Roy. Meteor. Soc.*, **126**, 1–30, doi:10.1002/qj.49712656202.

Dauhut, T., J.-P. Chaboureau, J. Escobar, and P. Mascart, 2015: Large-eddy simulation of Hector the convector making the stratosphere wetter. *Atmos. Sci. Lett.*, **16**, 135–140, doi:10.1002/asl2.534.

Del Genio, A. D., and J. Wu, 2010: The role of entrainment in the diurnal cycle of continental convection. *J. Climate*, **23**, 2722–2738, doi:10.1175/2009JCLI3340.1.

de Reus, M., and Coauthors, 2009: Evidence for ice particles in the tropical stratosphere from in-situ measurements. *Atmos. Chem. Phys.*, **9**, 6775–6792, doi:10.5194/acp-9-6775-2009.

de Rooy, W. C., and A. P. Siebesma, 2008: A simple parameterization for detrainment in shallow cumulus. *Mon. Wea. Rev.*, **136**, 560–576, doi:10.1175/2007MWR2201.1.

——, and ——, 2010: Analytical expressions for entrainment and detrainment in cumulus convection. *Quart. J. Roy. Meteor. Soc.*, **136**, 1216–1227, doi:10.1002/qj.640.

——, and Coauthors, 2013: Entrainment and detrainment in cumulus convection: An overview. *Quart. J. Roy. Meteor. Soc.*, **139**, 1–19, doi:10.1002/qj.1959.

Ferretti, R., and S. Gentile, 2009: A study of the triggering mechanisms for deep convection in the tropics using a mesoscale model: Hector events during SCOUT-O3 and TWP-ICE campaigns. *Atmos. Res.*, **93**, 247–269, doi:10.1016/j.atmosres.2008.11.004.

Frey, W., and Coauthors, 2014: Tropical deep convective life cycle: Cb-anvil cloud microphysics from high-altitude aircraft observations. *Atmos. Chem. Phys.*, **14**, 13 223–13 240, doi:10.5194/acp-14-13223-2014.

Glenn, I. B., and S. K. Krueger, 2014: Downdrafts in the near cloud environment of deep convective updrafts. *J. Adv. Model. Earth Syst.*, **6**, 1–8, doi:10.1002/2013MS000261.

Grabowski, W. W., and D. Jarecka, 2015: Modeling condensation in shallow nonprecipitating convection. *J. Atmos. Sci.*, **72**, 4661–4679, doi:10.1175/JAS-D-15-0091.1.

Gregory, D., J.-J. Morcrette, C. Jakob, A. M. Beljaars, and T. Stockdale, 2000: Revision of convection, radiation and cloud schemes in the ECMWF model. *Quart. J. Roy. Meteor. Soc.*, **126**, 1685–1710, doi:10.1002/qj.49712656607.

Holton, J. R., P. H. Haynes, M. E. McIntyre, A. R. Douglass, R. B. Rood, and L. Pfister, 1995: Stratosphere–troposphere exchange. *Rev. Geophys.*, **33**, 403–439, doi:10.1029/95RG02097.

Keenan, T. D., M. J. Manton, G. J. Holland, and B. R. Morton, 1989: The Island Thunderstorm Experiment (ITEX)—A study of tropical thunderstorms in the Maritime Continent. *Bull. Amer. Meteor. Soc.*, **70**, 152–159, doi:10.1175/1520-0477(1989)070<0152:TITESO>2.0.CO;2.

Khairoutdinov, M. F., and D. A. Randall, 2006: High-resolution simulation of shallow-to-deep convection transition over land. *J. Atmos. Sci.*, **63**, 3421–3436, doi:10.1175/JAS3810.1.

——, S. K. Krueger, C.-H. Moeng, P. A. Bogenschutz, and D. A. Randall, 2009: Large-eddy simulation of maritime deep tropical convection. *J. Adv. Model. Earth Syst.*, **1** (15), doi:10.3894/JAMES.2009.1.15.

Lafore, J.-P., and Coauthors, 1998: The Meso–NH Atmospheric Simulation System. Part I: Adiabatic formulation and control simulations. *Ann. Geophys.*, **16**, 90–109, doi:10.1007/s00585-997-0090-6.

Lane, T. P., M. J. Reeder, and T. L. Clark, 2001: Numerical modeling of gravity wave generation by deep tropical convection. *J. Atmos. Sci.*, **58**, 1249–1274, doi:10.1175/1520-0469(2001)058<1249:NMOGWG>2.0.CO;2.

Lebo, Z. J., H. Morrison, and J. H. Seinfeld, 2012: Are simulated aerosol-induced effects on deep convective clouds strongly dependent on saturation adjustment? *Atmos. Chem. Phys.*, **12**, 9941–9964, doi:10.5194/acp-12-9941-2012.

Liu, X. M., E. D. Rivière, V. Marécal, G. Durry, A. Hamdouni, J. Arteta, and S. Khaykin, 2010: Stratospheric water vapour budget and convection overshooting the tropopause: Modelling study from SCOUT-AMMA. *Atmos. Chem. Phys.*, **10**, 8267–8286, doi:10.5194/acp-10-8267-2010.

Nielsen, J. K., N. Larsen, F. Cairo, G. Di Donfrancesco, J. M. Rosen, G. Durry, G. Held, and J. P. Pommereau, 2007: Solid particles in the tropical lowest stratosphere. *Atmos. Chem. Phys.*, **7**, 685–695, doi:10.5194/acp-7-685-2007.

Noilhan, J., and S. Planton, 1989: A simple parameterization of land surface processes for meteorological models. *Mon. Wea. Rev.*, **117**, 536–549, doi:10.1175/1520-0493(1989)117<0536:ASPOLS>2.0.CO;2.

Pantillon, F., P. Mascart, J.-P. Chaboureau, C. Lac, J. Escobar, and J. Duron, 2011: Seamless MESO-NH modeling over very large grids. *C. R. Mec.*, **339**, 136–140, doi:10.1016/j.crme.2010.12.002.

Pinty, J.-P., and P. Jabouille, 1998: A mixed-phase cloud parameterization for use in a mesoscale non-hydrostatic model: Simulations of a squall line and of orographic precipitations. *Proc. Conf. on Cloud Physics*, Everett, WA, Amer. Meteor. Soc., 217–220.

Riehl, H., and J. S. Malkus, 1958: On the heat balance in the equatorial trough zone. *Geophysica*, **6**, 503–538.

Romps, D. M., and Z. Kuang, 2010: Do undiluted convective plumes exist in the upper tropical troposphere? *J. Atmos. Sci.*, **67**, 468–484, doi:10.1175/2009JAS3184.1.

Saito, K., T. Keenan, G. Holland, and K. Puri, 2001: Numerical simulation of the diurnal evolution of tropical island convection over the Maritime Continent. *Mon. Wea. Rev.*, **129**, 378–400, doi:10.1175/1520-0493(2001)129<0378:NSOTDE>2.0.CO;2.

Schlemmer, L., and C. Hohenegger, 2014: The formation of wider and deeper clouds as a result of cold-pool dynamics. *J. Atmos. Sci.*, **71**, 2842–2858, doi:10.1175/JAS-D-13-0170.1.

van Zanten, M. C., and Coauthors, 2011: Controls on precipitation and cloudiness in simulations of trade-wind cumulus as observed during RICO. *J. Adv. Model. Earth Syst.*, **3**, M06001, doi:10.1029/2011MS000056.

Varble, A., and Coauthors, 2014: Evaluation of cloud-resolving and limited area model intercomparison simulations using TWP-ICE observations: 1. Deep convective updraft properties. *J. Geophys. Res. Atmos.*, **119**, 13 891–13 918, doi:10.1002/2013JD021371.